An anti-bacterial porous shape memory self-adaptive stiffened polymer for alveolar bone regeneration after tooth extraction

Weijun Zhang [a,1], Meilin Yu [b,c,1], Yongqiang Cao [a], Zihan Zhuang [a], Kunxi Zhang [a,**], Dong Chen [b,c,***], Wenguang Liu [d,****], Jingbo Yin [a,*]

[a] Department of Polymer Materials, School of Materials Science and Engineering, Shanghai University, Shanghai, 200444, China
[b] Department of Endodontics, Shanghai Stomatological Hospital & School of Stomatology, Fudan University, Shanghai, 200001, China
[c] Shanghai Key Laboratory of Craniomaxillofacial Development and Diseases, Fudan University, Shanghai, 200001, China
[d] School of Material Science and Engineering, Tianjin Key Laboratory of Composite and Functional Materials, Tianjin University, Tianjin, 300350, China

ARTICLE INFO

ABSTRACT

The regeneration of alveolar bone after tooth extraction is critical for the placement of dental implants. Developing a rigid porous scaffold with defect shape adaptability is of great importance but challenging for alveolar bone regeneration. Herein, we design and synthesize a biocompatible poly(L-glutamic acid)-g-poly(ε-caprolactone) (PLGA-g-PCL) porous shape memory (SM) polymer. The PLGA-g-PCL is then copolymerized with acryloyl chloride grafted poly(ω-pentadecalactone) (PPDLDA) having a higher phase transition temperature than shape recovery temperature to maintain stiffness after shape recovery to resist chewing force. The hybrid polydopamine/silver/hydroxyapatite (PDA/Ag/HA) is coated to the surface of (PLGA-g-PCL)-PPDL scaffold to afford the anti-bacterial activity. The porous SM scaffold can be deformed into a compact size and administered into the socket cavity in a minimally invasive mode, and recover its original shape with a high stiffness at body temperature, fitting well in the socket defect. The SM scaffold exhibits robust antibacterial activity against *Staphylococcus aureus* (*S. aureus*). The porous microstructure and cytocompatibility of PLGA allow for the ingrowth and proliferation of stem cells, thus facilitating osteogenic differentiation. The micro-CT and histological analyses demonstrate that the scaffold boosts efficient new bone regeneration in the socket of rabbit mandibular first premolar. This porous shape memory self-adaptive stiffened polymer opens up a new avenue for alveolar bone regeneration.

1. Introduction

Alveolar bone regeneration after tooth extraction is vital for denture implantation and aesthetic restoration [1,2]. Current studies have focused on the design of biomaterials capable of promoting bone regeneration to keep the morphology and quality of the alveolar bone. However, in consideration of oral microenvironments, such as irregular socket defect, bacteria breeding and chewing force, developing desirable biomaterials is still under challenges. Thermally-induced shape memory (SM) scaffolds can change shape in response to temperature stimuli [3,

4]. Their shape memory behavior ensures them to fit precisely into the bone defects through volume expansion, which holds great potential in alveolar bone regeneration. Nonetheless, most SM scaffolds reported thus far become weak after shape recovery [5–8]. Thus, there is a critical need to develop SM scaffolds that can maintain mechanical properties after shape recovery to facilitate alveolar bone regeneration.

A common approach to improving the mechanical strength of SM scaffolds is to increase the rigidity of the materials. Polymers with phase transition temperature higher than shape recovery temperature (T_r) have been shown to enhance the rigidity of the scaffolds after shape

recovery [9,10]. Poly(ω-pentadecalactone) (PPDL), a biodegradable polyester with a higher phase transition temperature (60–80 °C) [11], has great potential in the development of stiffened SM scaffolds. Nonetheless, to the best of our knowledge, the SM scaffold has not been harnessed to regenerate alveolar bone.

Since the oral cavity is populated by several microorganisms, the anti-bacterial property is another critical factor for the prevention of implant-related infection [12]. Silver ion (Ag^+) is well known for its wide spectrum anti-bacterial activity and has been extensively applied in clinical treatment of tooth decay [13]. However, due to the dose-dependent cytotoxicity of Ag^+, the rapid release may bring about a negative impact on proliferation, differentiation of stem cells and further implant osseointegration [14]. Polydopamine (PDA) immobilized silver/hydroxyapatite (Ag/HA) hybrid coating has been reported to modify bone grafts, thus allowing for the sustainable release of Ag^+, meanwhile improving cell proliferation and osteointegration [15–17]. Therefore, we hypothesize that stiffened SM scaffolds modified with PDA/Ag/HA hybrid coating may possess an impressive comprehensive performance, addressing the major problems associated with alveolar bone regeneration.

Poly(L-glutamic acid) (PLGA) is a synthetic polypeptide with protein mimic secondary structure, biocompatibility and biodegradability [18]. Our previous study on poly(L-glutamic acid)/poly(ε-caprolactone) (PLGA/PCL) porous SM scaffold has demonstrated its promising prospects in tissue regeneration [19]. However, its weak strength after shape recovery limited its application as an alveolar bone scaffold. In this study, a stiffened poly(L-glutamic acid)-g-poly(ε-caprolactone) (PLGA-g-PCL) porous SM scaffold with self-adaptive and anti-bacterial functions is reinforced by acryloyl chloride grafted poly(ω-pentadecalactone) (PPDLDA) whose surface is further modified by PDA/Ag/HA hybrid coating (Fig. 1). We anticipate that the (PLGA-g-PCL)-PPDL scaffold can well fit in the irregular socket defect at the temporary state and maintain high mechanical strengths after shape recovery to resist chewing force. The anti-bacterial activity of PDA/Ag/HA coating can prevent oral infection. In addition, porous microstructure and PLGA with high cellular affinity will allow for ingrowth and proliferation of stem cells, thus facilitating osteogenic differentiation to boost alveolar bone regeneration. This porous shape memory self-adaptive stiffened polymer is explored for the first time as the bio-scaffold for alveolar bone regeneration.

2. Results and discussion

2.1. Body-temperature responsive PLGA-g-PCL porous SM scaffolds

In this study, we constructed a porous SM scaffold through free radical crosslinking between PLGA-g-PCL and PPDLDA under ultraviolet (UV) irradiation and modified solvent-casting/particulate leaching (SCPL) protocol. The chemical structure of PLGA-g-PCL and PPDLDA was confirmed by ^{1}H Nuclear Magnetic Resonance (^{1}H NMR) spectra (Figs. S1 and S2). Accordingly, the molecular weight of PCL and PPDL was determined to be 3500 and 2000 g mol^{-1}, respectively; grafting ratio of PLGA-g-PCL and PPDLDA was 56% and 100% (Table S1). The cross-linking reaction occurred via free radical crosslinking between the
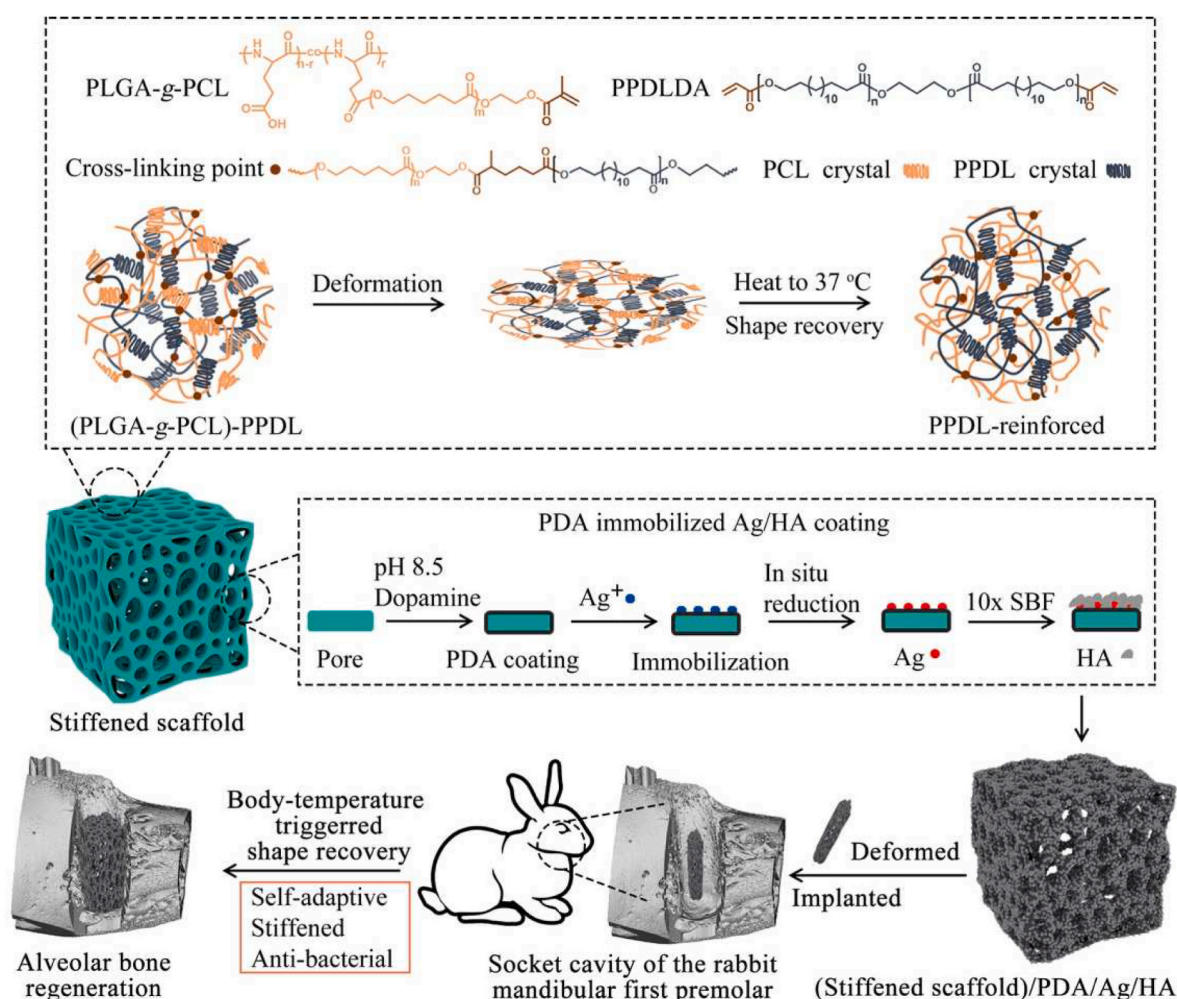

Fig. 1. Illustration of stiffened SM scaffolds with self-adaptive and anti-bacterial functions for alveolar bone regeneration.

PLGA-*g*-PCL and PPDLDA in the presence of I2959 as an initiator under UV (Fig. S3A). Gelation and mechanical property of cross-linked (PLGA-*g*-PCL)-PPDL gel were evaluated by oscillatory rheology [20]. Gel formation and storage modulus (G′) were both improved with the increase of UV irradiation period. As shown in Figs. S3B and S3C, increasing UV irradiation period (from 1 to 5 min) resulted in well-formed gel, with G' rising from 56 ± 19 Pa to 596 ± 40 Pa. Thus, free radical crosslinking between PLGA-*g*-PCL and PPDLDA was successfully carried out within 5 min, which was employed for the further fabrication of the scaffolds.

Porous structure was prepared by a modified SCPL protocol where sodium chloride (NaCl) particles were added with a small amount of water to form a template (Fig. 2A) [21]. Pore morphology, size and porosity of the scaffolds can be adjusted by the weight percentage of added water and observed by Scanning Electron Microscope (SEM). As shown in Fig. 2B, the addition of 2.5 wt% water led to more interconnected pores. Although interconnectivity further increased with the addition of 5 wt% water, the porous structure became fragile. Both pore size and porosity of the scaffolds decreased and increased with adding more water, respectively. With the addition of 0, 2.5 and 5 wt% water, the pore sizes were 490, 410 and 300 μm (Fig. 2C), the porosities were 79%, 91% and 95% (Fig. 2D). Compared with conventional SCPL which generates closed-cell foams with poor interconnectivity, the modified SCPL was utilized to produce scaffolds with highly interconnected porous structures, which is beneficial for mass transport and heat transfer through water convection. In order to obtain scaffolds with good interconnectivity and intact pore structure, modified SCPL with water addition of 2.5 wt% was determined to fabricate the porous scaffolds.

To achieve body-temperature response, the T_r of the porous scaffold was regulated by the mass ratio of PLGA-*g*-PCL and PPDLDA, including 90:10, 70:30, 50:50, 30:70 and 10:90. Gel fraction was carried out in advance to evaluate the free radical cross-linking of these scaffolds. No significant difference in cross-linking density was found (Fig. S4) [22]. Then, the thermal properties of the scaffolds were characterized by Differential Scanning Calorimetry (DSC) (Fig. 2E). In the DSC measurement, the lower melt peak was attributed to PCL as T_r, and the higher melt peak belonged to PPDL. All scaffolds exhibited T_r except the one with a polymer mass ratio of 10:90, which is due to the low PCL content. Moreover, T_r varied from 36 to 44 °C showing the dependence on polymer content (Table S2) [23]. Although T_r of scaffolds with polymer mass ratios 30:70 and 50:50 was close to the body temperature, the crystalline degree of the former scaffold was only 6% (Table S2), which was not conducive to fixing the temporary shape. Therefore, the body-temperature responsive porous SM scaffolds were finally fabricated by a polymer mass ratio of 50:50.

2.2. Mechanical reinforcement of SM scaffolds

SM polymers without any reinforcement exhibited unsatisfied mechanical strength at T_r, which greatly limits their applications, especially in load-bearing tissues [24]. Nanofillers such as hydroxyapatite, carbon nanotubes and graphene oxide as a rigid structure, have been applied to enhance the mechanical properties of porous SM scaffolds [25–27]. However, due to interface compatibility between polymers and
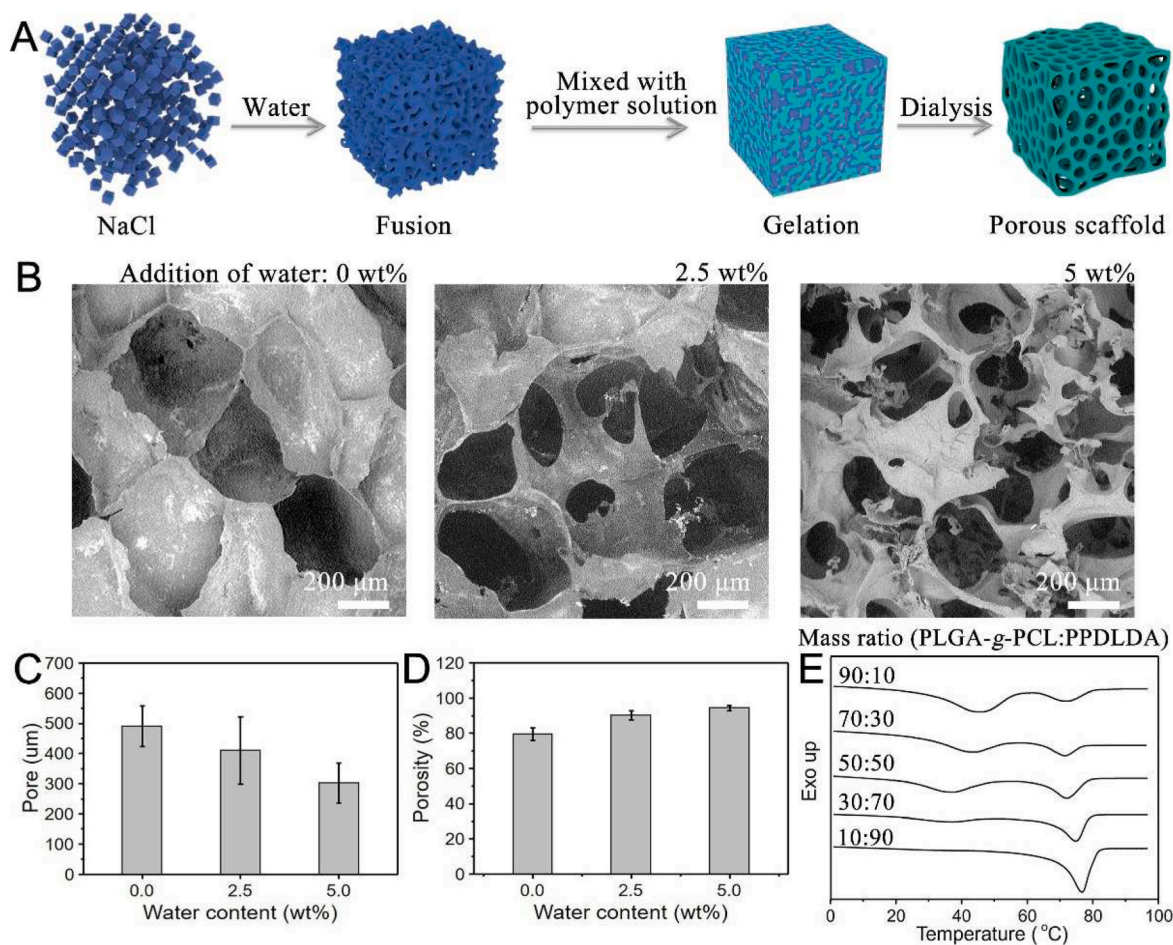
Fig. 2. Fabrication of body-temperature responsive PLGA-*g*-PCL porous SM scaffolds. (A) Illustration of modified SCPL protocol. (B) SEM images of the porous structure. (C) pore size and (D) porosity affected by salt fusion with different water addition. (E) DSC curves of scaffolds fabricated by the different mass ratios of PLGA-*g*-PCL and PPDLDA. All statistical data are represented as mean $\pm$ SD (n = 3, **$P < 0.01$).

nanofillers and the feature of porous structure, the strength at T_r is far from meeting demand.

It's worth noting that a rigid structure, constructed by the hydrophobic assembly of amphiphilic polymers, could have an efficient improvement on mechanical properties of SM polymers [9]. Inspired by this, a stiffened SM scaffold ((PLGA-*g*-PCL)-PPDL scaffold) was constructed by the introduction of PPDLDA copolymerized with PLGA-*g*-PCL. Depending on the higher melting temperature (T_m), PPDL could act as a rigid structure to strengthen the scaffold after shape recovery. Mechanical properties were detected by Dynamic Thermomechanical Analyzer (DMA). The unreinforced SM scaffolds (PLGA-*g*-PCL scaffold) showed a drastic decrease in compression strength and Young's modulus at T_r, which reduced from 0.15 to 0.05 MPa and 2.6 to 0.1 kPa, respectively (Fig. 3A–C). Although the mechanical properties were also reduced at T_r, ((PLGA-*g*-PCL)-PPDL) scaffolds still exhibited 0.13 MPa in compression strength and 1.0 kPa in Young's modulus with the introduction of PPDL (Fig. 3A–C), which was 2.6-fold and 10-fold higher than PLGA-*g*-PCL scaffolds. As demonstrated in Fig. 3D, PLGA-*g*-PCL scaffolds collapsed to 25% of their original

height under a 50 g weight load at T_r (Fig. 3E). However, ((PLGA-*g*-PCL)-PPDL) scaffolds could remain 66% of the original height under the same condition (Fig. 3E). These results demonstrated that PPDL exhibited a positive effect on mechanical reinforcement of SM scaffolds at T_r. Interestingly, our results reached from 2-fold to 10-fold in compression strength compared with the reported reinforced porous SM scaffolds [25–27].

To better understand the mechanism of PPDL reinforcement, scaffolds were immersed in dimethyl sulfoxide (DMSO) to ease the PCL crystals, simulating the temperature stimulation. As shown in Fig. S5A, PLGA-*g*-PCL scaffolds became soft and transparent, while ((PLGA-*g*-PCL)-PPDL) scaffolds kept still rigid and semitransparent (Fig. S5B). To reveal the effect of the microstructure on mechanical properties, X-ray Diffractometer (XRD) and Polarizing Optical Microscope (POM) were carried out. As demonstrated in Fig. 3F, PCL and PPDL exhibited similar diffraction peaks at $2\theta = 21.3°$ and $23.8°$ [28]. The relative peak intensity reduced as the temperature rose to T_r, which meant PCL crystals melted but PPDL crystals were preserved. This result was consistent with POM images that the birefringence of the PLGA-*g*-PCL scaffolds
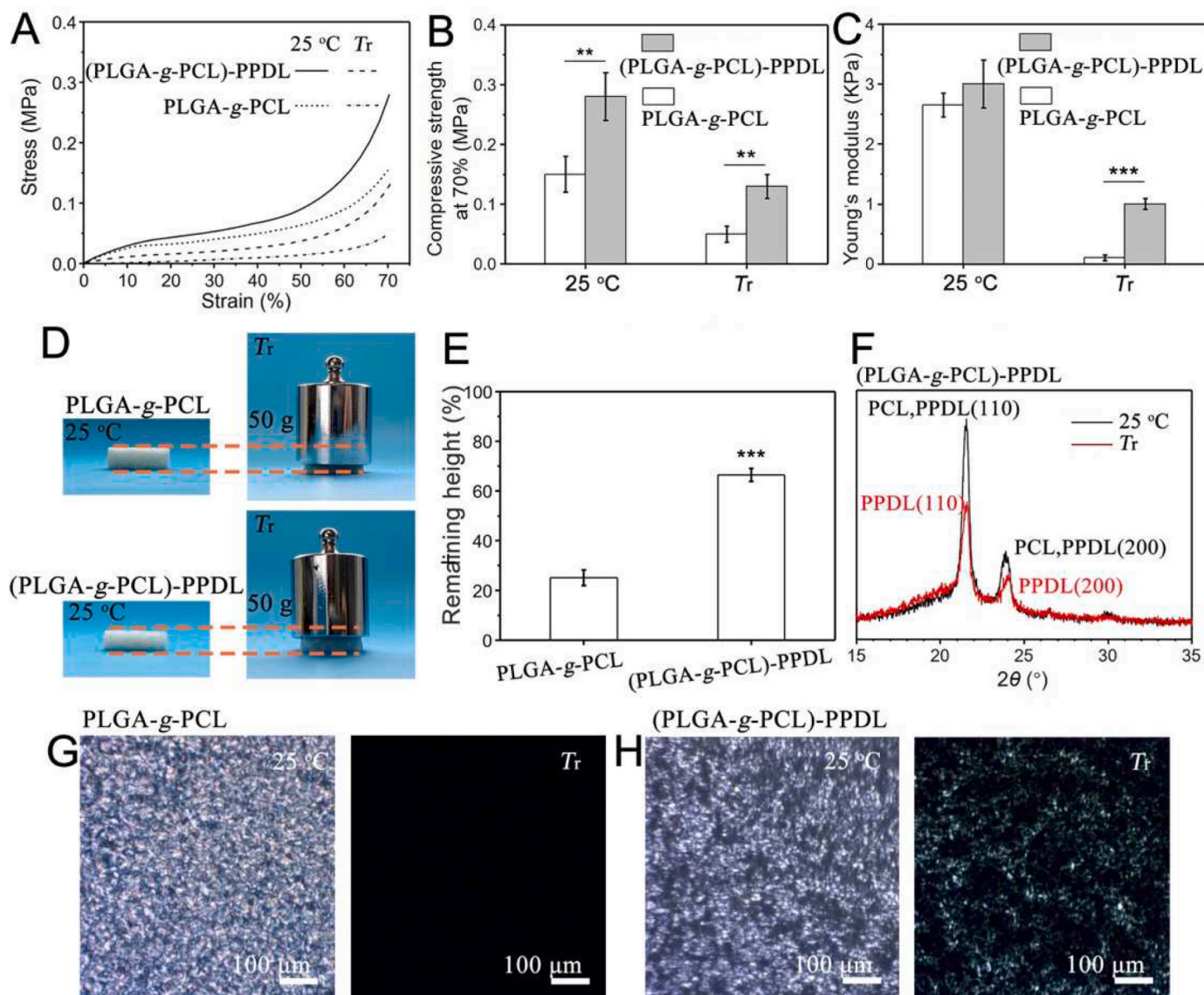
Fig. 3. Analysis of mechanical properties and mechanism of stiffened SM scaffolds ((PLGA-*g*-PCL)-PPDL scaffolds) and unreinforced SM scaffolds (PLGA-*g*-PCL scaffolds). (A) DMA curves. (B) compression strength. (C) Young's modulus. (D) Digital images. (E) percentage of the remaining height of scaffolds under 50 g weight load. (F) XRD curves of stiffened SM scaffolds ((PLGA-*g*-PCL)-PPDL). POM images of (G) PLGA-*g*-PCL network and (H) (PLGA-*g*-PCL)-PPDL network at 25 °C and T_r. All statistical data are represented as mean ± SD (n = 3, **$P < 0.01$, ***$P < 0.001$).

disappeared at T_r (Fig. 3G) but remained in ((PLGA-*g*-PCL)-PPDL) scaffolds (Fig. 3H). Collectively, these findings indicated that PPDL crystal could act as a rigid structure to enhance the mechanical properties of porous SM scaffolds at T_r.

2.3. Surface modification of stiffened scaffolds with PDA/Ag/HA hybrid coating

For the prevention of oral infection, the anti-bacterial ability is an indispensable attribute for the materials employed in the clinical application. PDA immobilized Ag/HA hybrid coating has been employed to functionalize bone grafts, such as osteoconduction, anti-bacterial activity and osseointegration [16]. In this work, the PDA coating was formed on stiffened scaffolds by universal immersion of the scaffolds in dopamine/Tris-HCl solution (2 mg mL^{-1}, pH 8.5) [29]. The covalent oxidative polymerization and cross-linking of PDA occurred on the scaffold through pH-induced oxidization. Compared with unmodified scaffolds (Figs. S6A and S6B), the deposited PDA coating apparently increased the surface roughness (Figs. S6C and S6D). Then, the (stiffened scaffold)/PDA was immersed in 0.1 mM silver nitrate (AgNO$_3$) solution for the deposition of Ag to fabricate (stiffened scaffold)/PDA/0.1Ag. In this process, Ag$^+$ were adsorbed on the surface of scaffolds via the co-ordination reaction between Ag$^+$ and catechol groups of PDA. The Ag$^+$ was then in-situ reduced to metallic Ag by redox activity of catechol groups, which resulted in Ag clusters or aggregates on the scaffold (Figs. S6E and S6F) [30]. Energy-dispersive X-ray (EDX) analysis in Figs. S6b, 6d, 6f and Table S3 further indicated the deposition of Ag on the scaffold surface.

After that, the samples were finally functionalized by mineralization in 10 × SBF. SEM and EDX images of (stiffened scaffold)/PDA/0.1Ag/HA were shown in Fig. 4A–C. After mineralization, the scaffolds were significantly covered by spherical minerals, whose mean content is 16.8% (Fig. S7). Ca/P ratio 1.61 was close to the stoichiometric ratio of HA (Ca/P = 1.67, Ca$_{10}$(PO$_4$)$_6$(OH)$_2$), indicating that the polydopamine layers provided sufficient catechol groups available for CaP nucleation [31]. EDX analysis indicated that Ag and C content decreased after mineralization, with significantly increased O, Ca and P content (Table S3). The (stiffened scaffold)/PDA/0.1Ag/HA was also subjected to XRD analysis to determine the phase composition. As shown in Fig. 4D, diffraction peaks at $2\theta = 21.3°$ and $23.8°$ belonging to the (110) and (200) crystal faces of PCL and PPDL [28]; three diffraction peaks were identified at $31.6°$, $38.1°$, $44.3°$ in the pattern of the scaffolds after Ag deposition, indicating the presence of cubic metallic Ag [30]; two obvious diffraction peaks of HA were finally observed at $25.9°$ and $32.0°$ [32]. Taken together, these results indicated that stiffened scaffolds were successfully modified with PDA/Ag/HA hybrid coating.
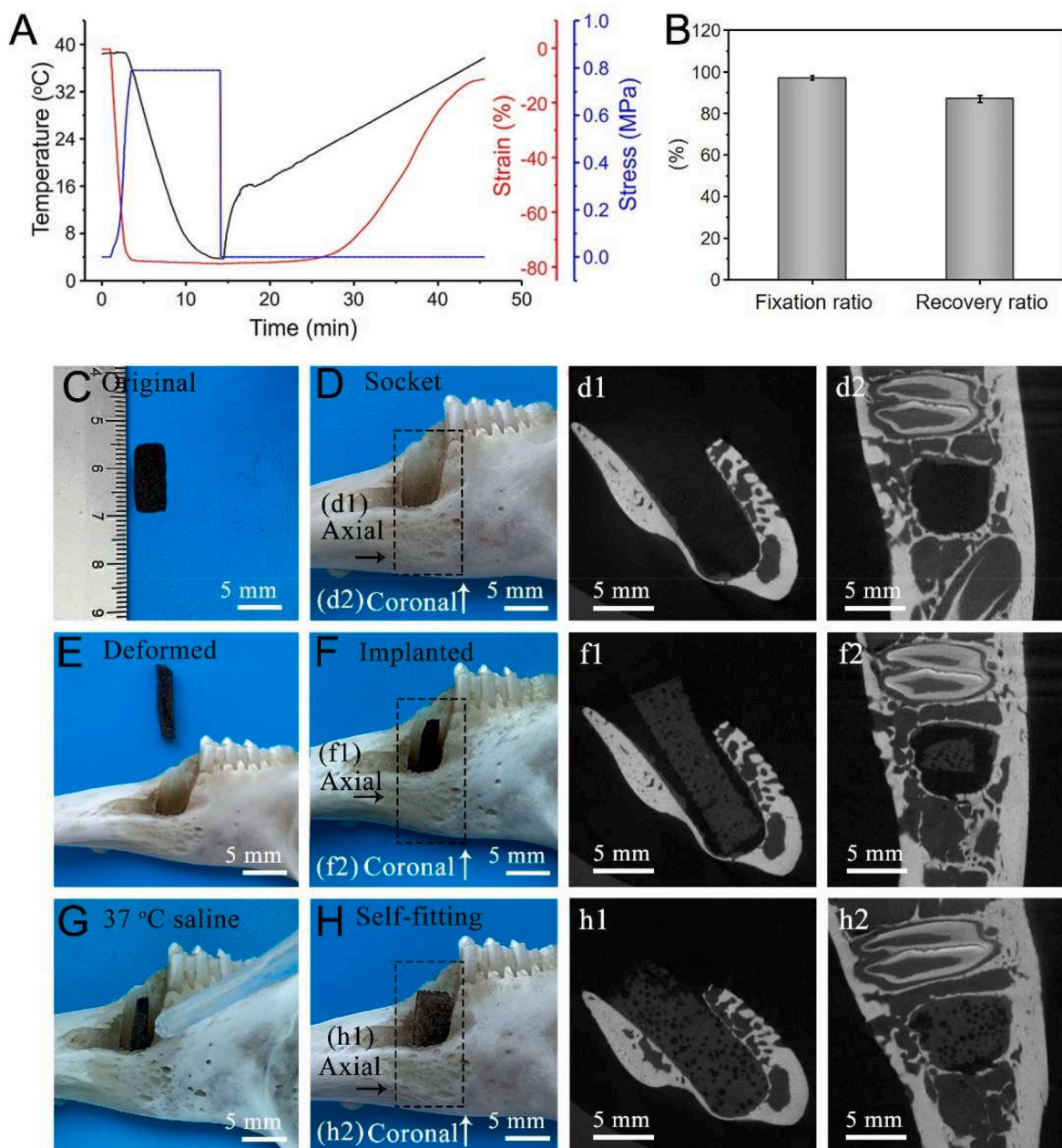
2.4. Shape memory and self-adaptive functions

After tooth extraction, filling the void in a convenient way has become an unavoidable issue for materials implantation [33]. The unique advantage of porous SM scaffold is that it can fill defects under body temperature with the recovered porous structure which makes the materials easier to be implanted.

Here we presented a body-temperature responsive porous (stiffened scaffold)/PDA/0.1Ag/HA SM scaffold. To confirm whether the scaffold has a good shape memory function in response to body temperature, the shape fixation ratio (R_f) and shape recovery ratio (R_r) were investigated. From the DMA curves (Fig. 5A), samples were compressed to a strain of 80% at 37 °C, cooled to 5 °C, unloaded to fixation and gradually heated to 37 °C, showing the shape recovery. R_f and R_r values of the porous scaffold exceeded 97% and 87%, respectively (Fig. 5B). In addition, the shape memory process is shown in Fig. S8A. The scaffold was compressed at 37 °C and cooled to 0 °C to fix a temporary shape. Later, the scaffold was submerged in 37 °C saline and recovered.

We further evaluated the self-adaptive performance of the SM
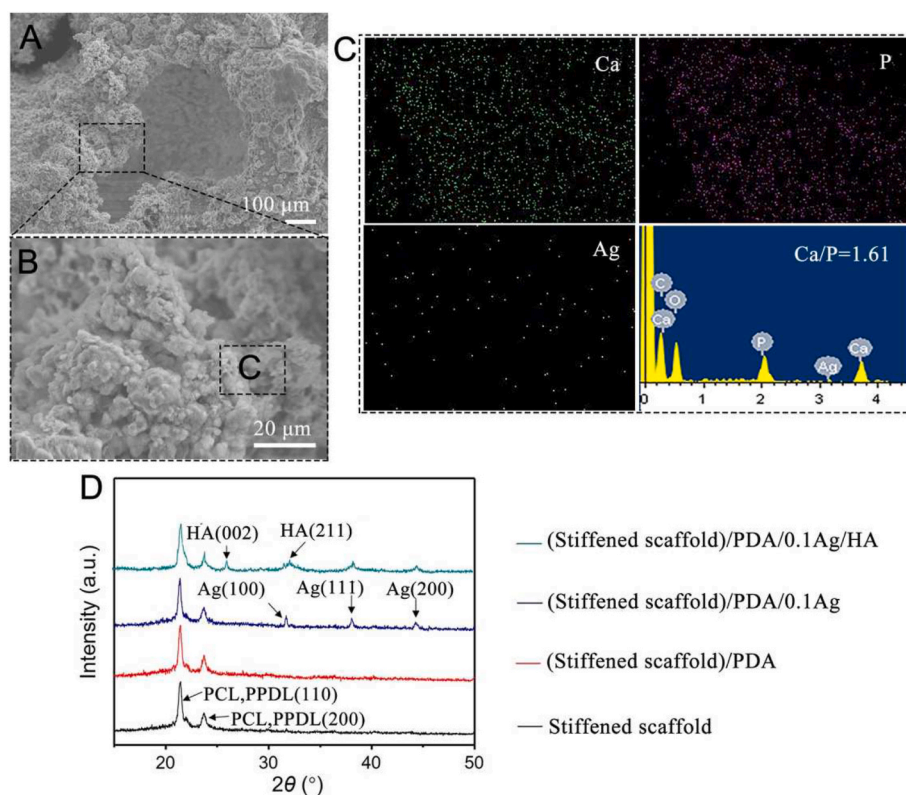
Fig. 4. Fabrication of stiffened scaffolds with PDA/0.1Ag/HA hybrid coating. (A) SEM images. (B) Magnification of (A). (C) EDX analysis of Ca, P, Ag. (D) XRD curves.

Fig. 5. Shape memory and self-adaptive functions of the (stiffened scaffold)/PDA/0.1Ag/HA. (A) DMA curves. (B) Shape fixation ratio (R_f) and recovery ratio (R_r). *In vitro* simulation of socket filling. (C) An original scaffold. (D) The socket of the rabbit mandibular first premolar. (E) A deformed scaffold. (F) A scaffold implanted into the socket. (G) Adding 37 °C saline. (H) A scaffold was recovered to fill the socket triggered by 37 °C saline. (d1), (d2), (f1), (f2), (h1) and (h2) are representative two-dimensional micro-CT images of (D), (F) and (H). All statistical data are represented as mean ± SD (n = 3).

scaffolds *in vitro*. The implantation of the deformed scaffold is shown in Fig. 5C–H. At first, the scaffold was deformed into a compact shape that is easier to implant into the socket of the rabbit's mandibular first pre-molar. Then, 37 °C saline for the simulation of the physiological environment was added to the defect. In the end, the scaffold quickly recovered to its original shape to fill the socket. To analyze whether the scaffold can integrate with the socket, the micro-CT analysis, viewed from the axial and coronal direction, was employed [5]. As shown in Figs. 5d1 and 5d2, the socket was empty before implantation. After the insertion of deformed scaffolds (Figs. 5f1 and 5f2), the void could be well filled after shape recovery of the scaffold (Figs. 5h1 and 5h2).

The way of porous shape memory scaffolds filling irregular defects mainly depends on volume expansion during shape recovery [5]. As shown in Fig. S8B, the scaffold of a square shape (1.4 × 1.4 mm) not only

could fill and adapt to a round shape inner the tube (Φ1.2 mm) after shape recovery but also would not fall out. It was reported that inject-able hydrogels were difficult to be handled with higher viscosity but easier to leak from the larger defect with unsatisfied mechanical strength [34]. In the contrast, our stiffened SM scaffolds could maintain stability in the defect, indicating the scaffold was a surgically friendly biomaterial. Taken together, the scaffold possesses a good shape memory function and self-adaptability at body temperature for the potential application in alveolar bone defect implantation.

2.5. In vivo degradation and tissue invasion

Scaffolds that support tissue invasion are beneficial for neo-tissue formation [35]. In this study, (stiffened scaffold)/PDA/0.1Ag/HA was

implanted subcutaneously to study the tissue invasion. According to the H&E staining images in Fig. 6A, plenty of subcutaneous tissue has already invaded the pores of the scaffolds after 1-month post-implantation, indicating that the porous scaffolds supported tissue invasion. After 2 months (Fig. 6C), the situation remained unchanged until 3 months later. The *trans*-pore growth of invaded tissue within the scaffold indicated a further extent of tissue invasion occurred accompanying scaffold degradation (Fig. 6E).

Besides tissue invasion, scaffolds should be biodegradable so as to be eventually replaced by neo-tissue [36]. The remaining weight of the scaffold after 1-, 2- and 3-months of *in vivo* degradation was 95%, 83% and 68% respectively (Fig. S9). In addition, in comparison to the hematoxylin-eosin (H&E) staining images (Figs. 6A, 6C and 6E), the dark purple portion along with the pore structure gradually lightens with time, which may be related to the degradation of the hybrid coating. After tissue removal, the hybrid coating of the scaffolds was further characterized by SEM and EDX. As shown in Fig. 6B and b1, after 1 month of *in vivo* degradation, plenty of HA is still presented on the surface of the scaffold. However, at 2 months, HA reduced and the pore wall was partially exposed (Figs. 6D and 6d1). After 3 months of degradation, the morphology of HA on the surface of the scaffold transformed from original dense coverage to an island-like distribution (Figs. 6F and 6f1), corresponding to the reduction of the dark purple portion in the H&E image (Fig. 6E), indicating that HA slowly dissolved. EDX analysis in Figs. 6b2, 6d2, 6f2 and Table S4 indicated that Ag was difficult to be detected after 1 month, which may be attributed to the release behavior needs to be further characterized.

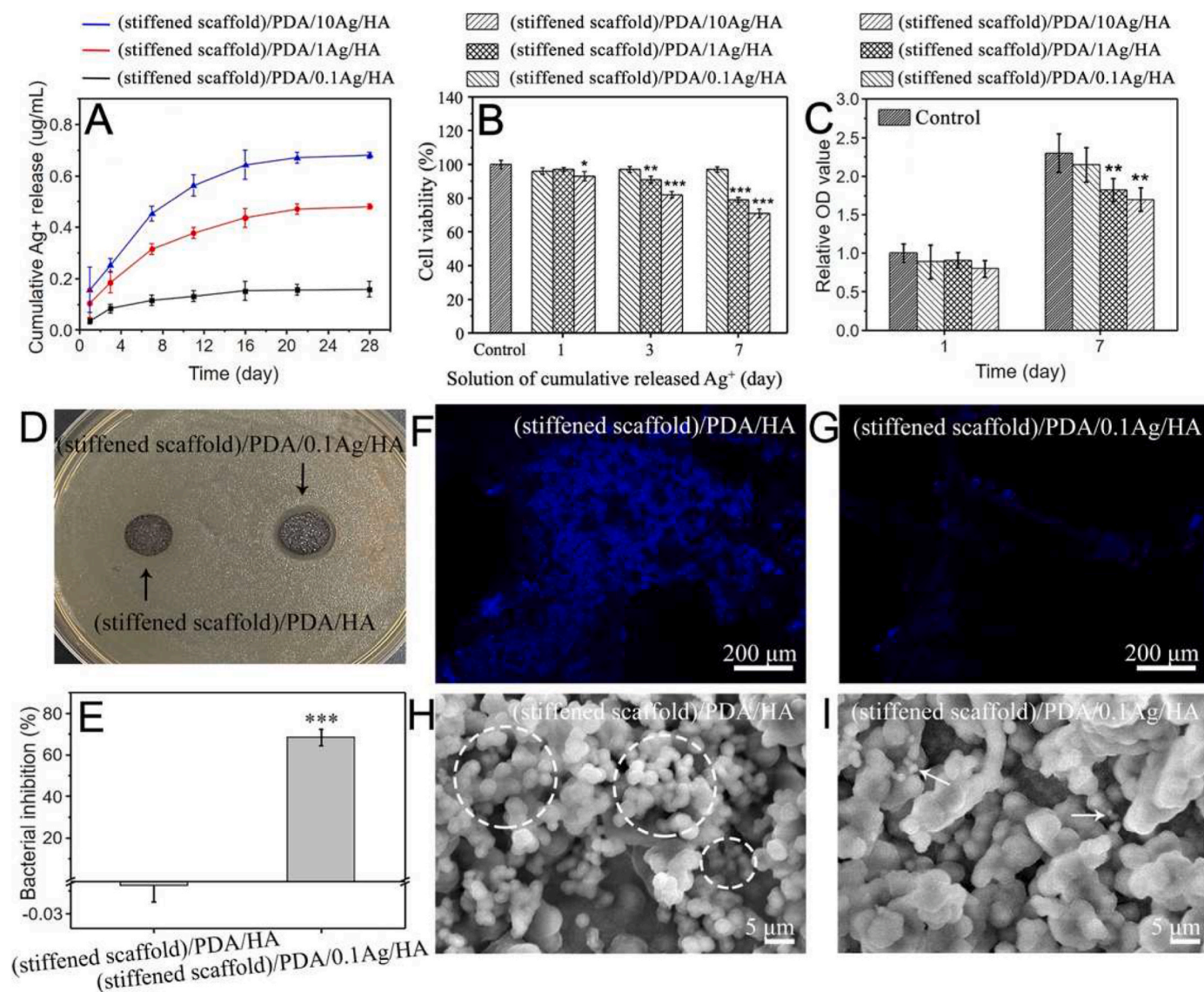## 2.6. Ag $^+$ release, cytotoxicity and anti-bacterial properties

It is well recognized that Ag$^+$ has broad antibacterial properties and less potential in antibacterial resistance [37]. It is reported that the reaction between oxygen (O$_2$), hydrogen ions (H$^+$) and Ag results in Ag$^+$ release from Ag-loaded materials, which leads to anti-bacterial activity [38]. However, owing to the highly dose-dependent cytotoxicity, controlling the concentration of released Ag$^+$ is very important to ease the negative effect on cell behaviors and implant osseointegration [39].

In order to achieve a balance between cytotoxicity and antibacterial properties, scaffolds fabricated in 0.1, 1 and 10 mM AgNO$_3$ and named by (stiffened scaffold)/PDA/0.1Ag/HA, (stiffened scaffold)/PDA/1Ag/HA and (stiffened scaffold)/PDA/10Ag/HA were employed to determine an optimal Ag$^+$ concentration. Firstly, the amount of Ag deposited on scaffolds was analyzed by Thermal Gravimetric Analyzer (TGA) (Fig. S10A). The remaining weight of samples increased with the amount of deposited Ag. In detail, the Ag content of (stiffened scaffold)/PDA/0.1Ag/HA, (stiffened scaffold)/PDA/1Ag/HA and (stiffened scaffold)/PDA/10Ag/HA was 0.67, 1.08 and 2.25 wt%, respectively (Fig. S10B). Then, the accumulated release of Ag$^+$ over 28 days is shown in Fig. 7A. The cumulative concentration of Ag$^+$ gradually increased within 11 days and became steady after 16 days, which may be resulted in undetectable Ag content after 1-month degradation *in vivo*. The corresponding accumulated Ag $^+$ concentration of (stiffened scaffold)/PDA/0.1Ag/HA, (stiffened scaffold)/PDA/1Ag/HA and (stiffened scaffold)/PDA/10Ag/HA was 0.16, 0.48 and 0.68 μg mL^{-1}, respectively. The results ensure the scaffolds as a local Ag$^+$ delivery system.
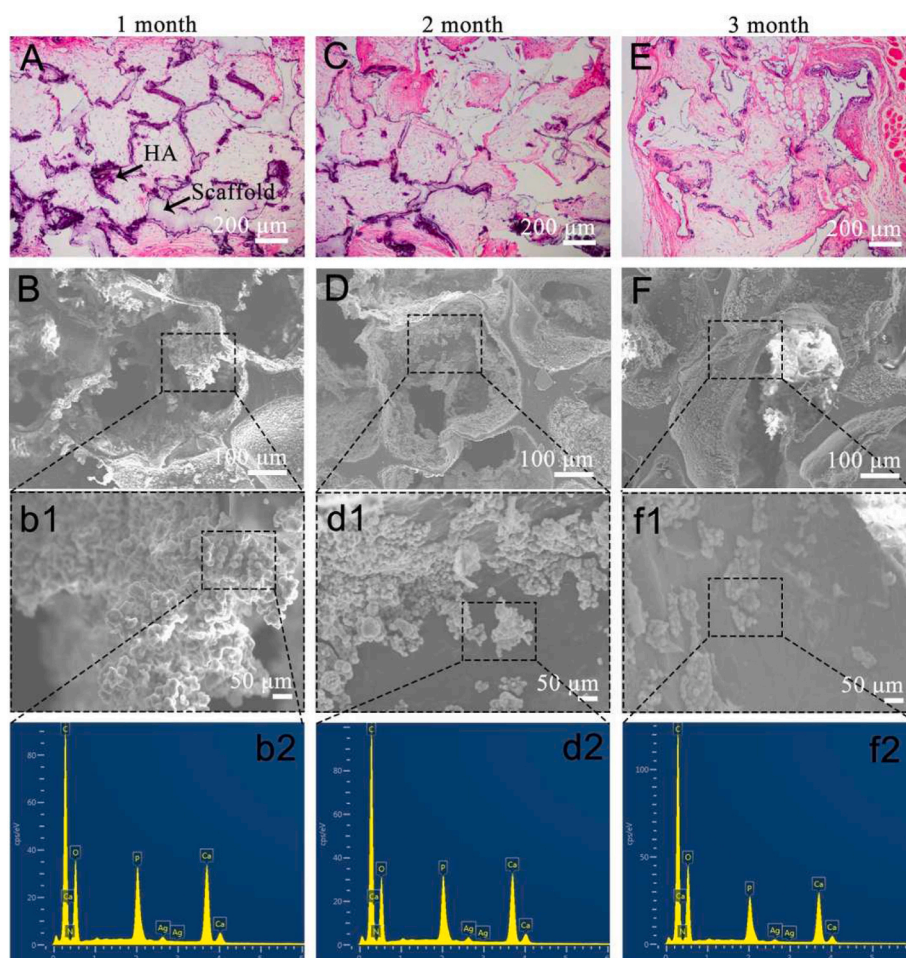
Fig. 6. *In vivo* degradation of (stiffened scaffold)/PDA/0.1Ag/HA. (A), (C), (E) H&E images and (B), (D), (F) SEM images after *in vivo* degradation for 1, 2 and 3 months. b1, d1 and f1 are the magnification of B, D and F, respectively. b2, d2 and f2 are the EDX analysis of b1, d1 and f1, respectively.

Fig. 7. Release, cytotoxicity and anti-bacterial performance of Ag$^+$ from (stiffened scaffold)/PDA/0.1Ag/HA, (stiffened scaffold)/PDA/1Ag/HA and (stiffened scaffold)/PDA/10Ag/HA. (A) Cumulative release of Ag$^+$. (B) Cytotoxicity evaluation of cumulative released Ag$^+$ by MTT. (C) BMSCs proliferation. (D) Inhibition rings. (E) Bacterial inhibition rate. (F) and (G) Fluorescent images (blue represents DAPI stained *S. aureus*) and (H) and (I) SEM images (*S. aureus* within white dotted circles and white arrows referring to) of *S. aureus* attachment on scaffolds. All statistical data are represented as mean ± SD (n = 3, *$P < 0.05$, **$P < 0.01$, ***$P < 0.001$).

The release concentration of Ag$^+$ is the main reason for cytotoxicity. Fig. 7B showed the relative viabilities of Bone marrow stem cells (BMSCs) analyzed by MTT assay. Cell viability was reduced by 3 and 7 days' cumulative released Ag$^+$ form (stiffened scaffold)/PDA/1Ag/HA and (stiffened scaffold)/PDA/10Ag/HA. It is reported that Ag$^+$ in the range of 0.026–0.26 μg mL^{-1} resulted in efficient anti-bacterial property and the least cytotoxicity [39]. As shown in Fig. 7A, Ag$^+$ released from (stiffened scaffold)/PDA/1Ag/HA and (stiffened scaffold)/PDA/10Ag/HA came close or exceeded the range of 0.026–0.26 μg mL^{-1} after 3 days, while only (stiffened scaffold)/PDA/0.1Ag/HA kept Ag$^+$ concentration below 0.26 μg mL^{-1}, which resulted in the least effect on cell viability.

BMSCs were cultured on scaffolds with different Ag content to investigate the influence of Ag$^+$ concentration on cell proliferation. As demonstrated in Fig. 7C, BMSCs cultured on (stiffened scaffold)/PDA/1Ag/HA and (stiffened scaffold)/PDA/10Ag/HA were associated with reduced proliferation after culture for 7 days. (Stiffened scaffold)/0.1Ag/HA was associated with unaffected proliferation compared with

the control group.

(Stiffened scaffold)/PDA/0.1Ag/HA was also expected to exhibit potent anti-bacterial property. Thus, qualitative and quantitative investigations about the antibacterial activity of the scaffolds were performed. Samples were cultured with *Staphylococcus aureus* (*S. aureus*) for inhibition ring tests. It was apparent that (stiffened scaffold)/PDA/0.1Ag/HA had an obvious inhibition ring compared with (stiffened scaffold)/PDA/HA (Fig. 7D). Moreover, the bacterial inhibition rate against *S. aureus* of (stiffened scaffold)/PDA/0.1Ag/HA reached 68% after culture for 24 h, which was significantly higher than (stiffened scaffold)/PDA/HA (Fig. 7E). The morphology and distribution of the *S. aureus* on the surface of scaffolds were recorded by Laser Confocal Microscope (LCM) and SEM. As shown in Figs. 7F and 7G, much fewer bacteria stained by 4′,6-diamidino-2-phenylindole (DAPI) were observed on (stiffened scaffold)/PDA/0.1Ag/HA in LCM images. These results are consistent with SEM images (Figs. 7H and 7I). *S. aureus* were distributed at a high density on (stiffened scaffold)/PDA/HA, while relatively few bacteria were on (stiffened scaffold)/PDA/0.1Ag/HA.

Thus, the (stiffened scaffold)/PDA/0.1Ag/HA could inhibit *S. aureus* by sustained release of Ag^+.

2.7. Proliferation and osteogenic differentiation of BMSCs

Furthermore, the attachment and osteogenic differentiation of BMSCs on the (stiffened scaffold)/PDA/0.1Ag/HA were detected. The adhesion of BMSCs was observed by SEM and LCM. As shown in Figs. 8A and 8B, after 1-day culture, BMSCs could adhere to the surface of the scaffold and spread in a shuttle shape. The number of BMSCs increased with the culture period (Fig. S11). BMSCs and ECM covered the original three-dimensional pore structure after 14 days of culture. In addition, osteogenic differentiation of BMSCs was analyzed by Reverse Transcription-Polymerase Chain Reaction (RT-PCR) and Alizarin red S (ARS) staining (Figs. 8C and 8D). The data revealed that osteogenic genes, including alkaline phosphatase (ALP) and osteocalcin (OCN), as well as calcium nodules of BMSCs, increased with time. In general, (stiffened scaffold)/PDA/0.1Ag/HA supported adhesion, proliferation and osteogenic differentiation of BMSCs.
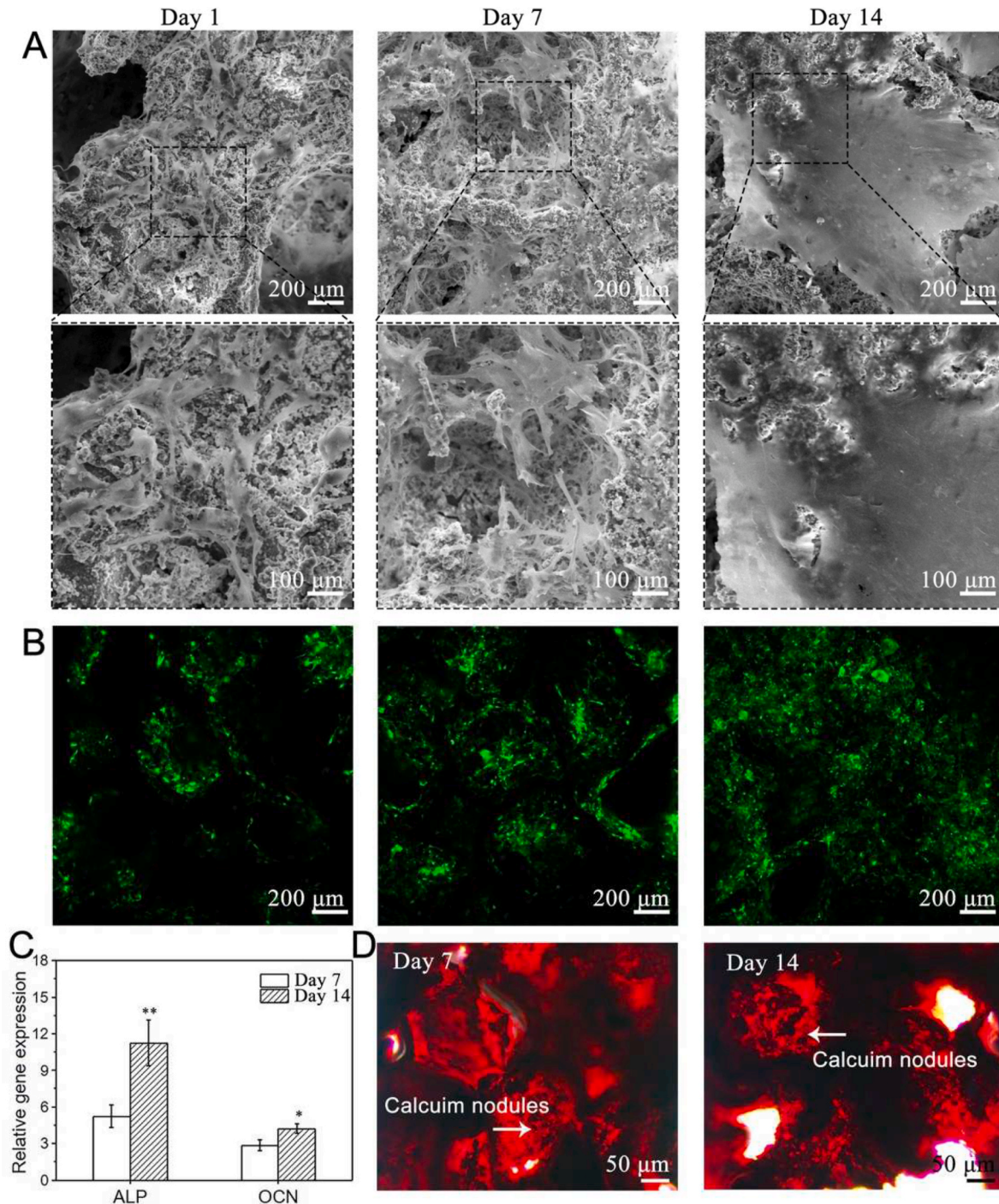
Fig. 8. Proliferation and osteogenic differentiation of BMSCs on (stiffened scaffold)/PDA/0.1Ag/HA. (A) SEM images. (B) Fluorescent images of DiO (green) labeled BMSCs. (C) Expression of osteogenic genes ALP and OCN determined by RT-PCR. (D) ARS staining (red) of calcium nodule. All statistical data are represented as mean ± SD (n = 3, *$P < 0.05$, **$P < 0.01$).

2.8. Alveolar bone regeneration

Repair of alveolar bone after tooth extraction is vital for further dental implant surgery [1,2]. The clinical data of the orthodontic force was about 10–120 g. After loading, (stiffened scaffold)/PDA/0.1Ag/HA exhibited better cell protective property than (unreinforced scaffold)/PDA/0.1Ag/HA (Fig. S12), which was more promising for further *in vivo* study [40]. Thus, in this study, (stiffened scaffold)/PDA/0.1Ag/HA was implanted into the socket of the rabbit mandibular first premolar with critical-sized defects (5 mm × 5 mm x 6 mm) for alveolar bone regeneration. After tooth extraction and drilling of a critical-sized defect, a deformed scaffold was implanted into the surgical place and shape recovered with body temperature as demonstrated in Fig. 4. Samples were collected after 1 and 2 months to evaluate osteogenesis *in vivo*. The defects were either filled with (stiffened scaffold)/PDA/0.1Ag/HA for the scaffold group or left unfilled for the blank group.

Through the observation of soft tissue (Fig. 9A), most of the gingival tissue healed after 1 month in the scaffold group. At 2 months, the gingiva around the socket healed well and there was no significant difference with the blank group, indicating the scaffold with good tissue affinity. Micro-CT was used to quantify bone regeneration. Representative 3D reconstructions of the axial-view micro-CT images were shown in Fig. 9B. After 1 month, new bone formed in the blank group and the bone trabeculae were mainly distributed around the socket, less new bone was observed in the central area. For the scaffold group, there was a small amount of new bone formation, which was mainly concentrated at the junction between the scaffold and the socket, down near the lower part of the socket. After 2 months, the scaffold group exhibited significantly greater X-ray radiopacity within the defect than the blank group. This suggested a larger new bone volume fraction (BV/TV in %), bone

mineral density (BMD in g/cc) and trabecular number (Tb.N in 1/mm) in the scaffold group, which was 1.4-fold, 1.3-fold and 1.2-fold compared to the blank group (Fig. 9C–E). To ascertain the possibility that the non-resorbed mineral coating on the scaffolds can contribute to the contrast in the X-ray micro-CT, histological analysis of the tissue sections from the two experimental groups was carried out.

Tissue sections of the blank group and scaffold group after 1 and 2 months were analyzed by H&E staining. After 1 month, compared to the blank group, new bone formation was localized to the periphery of the lower detect region in the scaffold group (Figs. 10A and 10B). At 2 months, a significant increase in new bone was both observed in both the blank and scaffold groups. However, the more trabecular bone could be obviously detected in the scaffold group. Importantly, the new bone formation was already more inclined to fill the defect and the percentage of new bone in the defect area was plotted in Fig. 10C. A significant difference was found at 2 months, the new bone area percentage of the scaffold group was 1.7-fold higher than that in the blank group. In summary, histology and micro-CT analysis together indicated such scaffold with comprehensive functions would possess great potential in alveolar bone regeneration after tooth extraction.

3. Conclusion

In summary, an anti-bacterial porous shape memory self-adaptive stiffened scaffold was explored for alveolar bone regeneration after tooth extraction. The scaffold, which was fabricated by copolymerization of PLGA-*g*-PCL with PPDL and PDA/Ag/HA hybrid coating modification, showed excellent shape memory and self-adaptive properties at body temperature. The mechanical strength and stiffness of the scaffold at T_r were enhanced by copolymerization with PPDL. The analysis of *in*
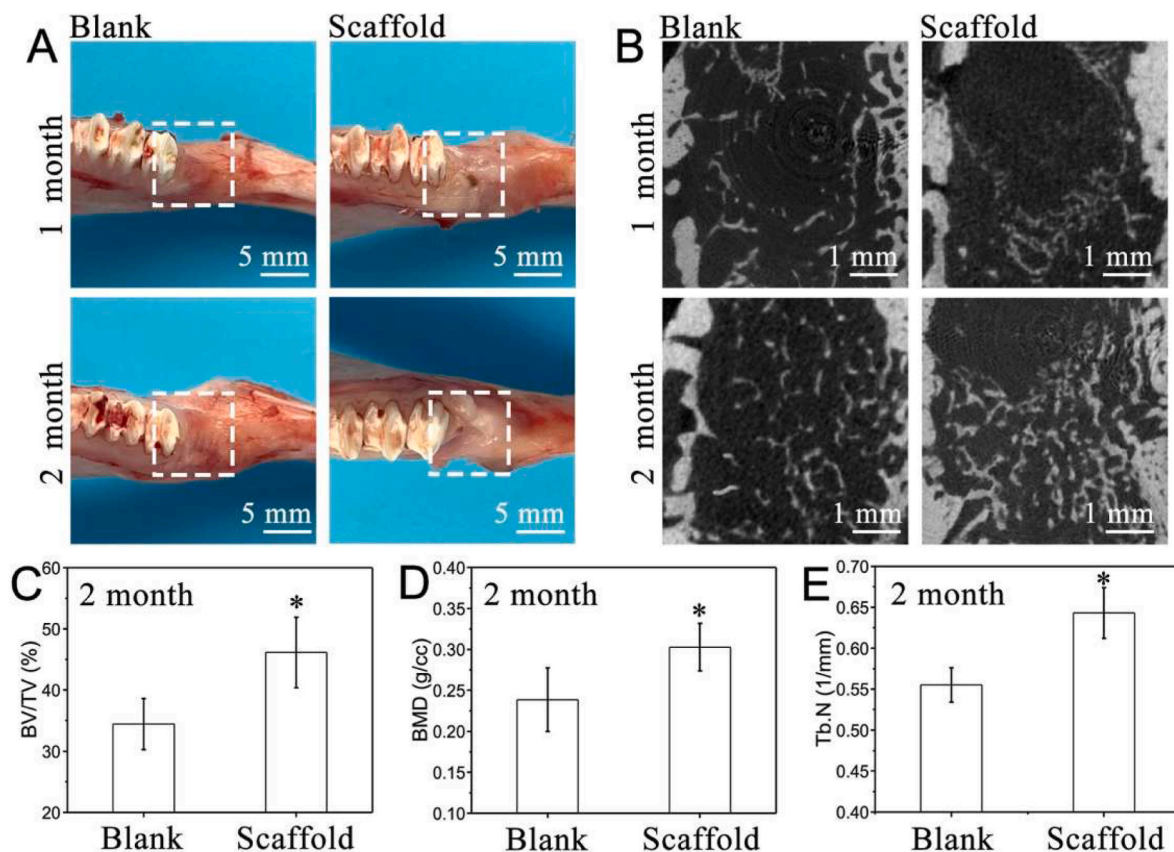
Fig. 9. Analysis of regenerated alveolar bone, the socket either was filled with (stiffened scaffold)/PDA/0.1Ag/HA (scaffold group) or left unfilled (blank group). (A) Digital images. (B) Representative two-dimensional micro-CT images. (C) Bone tissue volume/total tissue volume (BV/TV). (D) Bone mineral density (BMD) and (E) trabecular number (Tb.N) of blank group and scaffold group. All statistical data are represented as mean ± SD (n = 3, *$P < 0.05$).
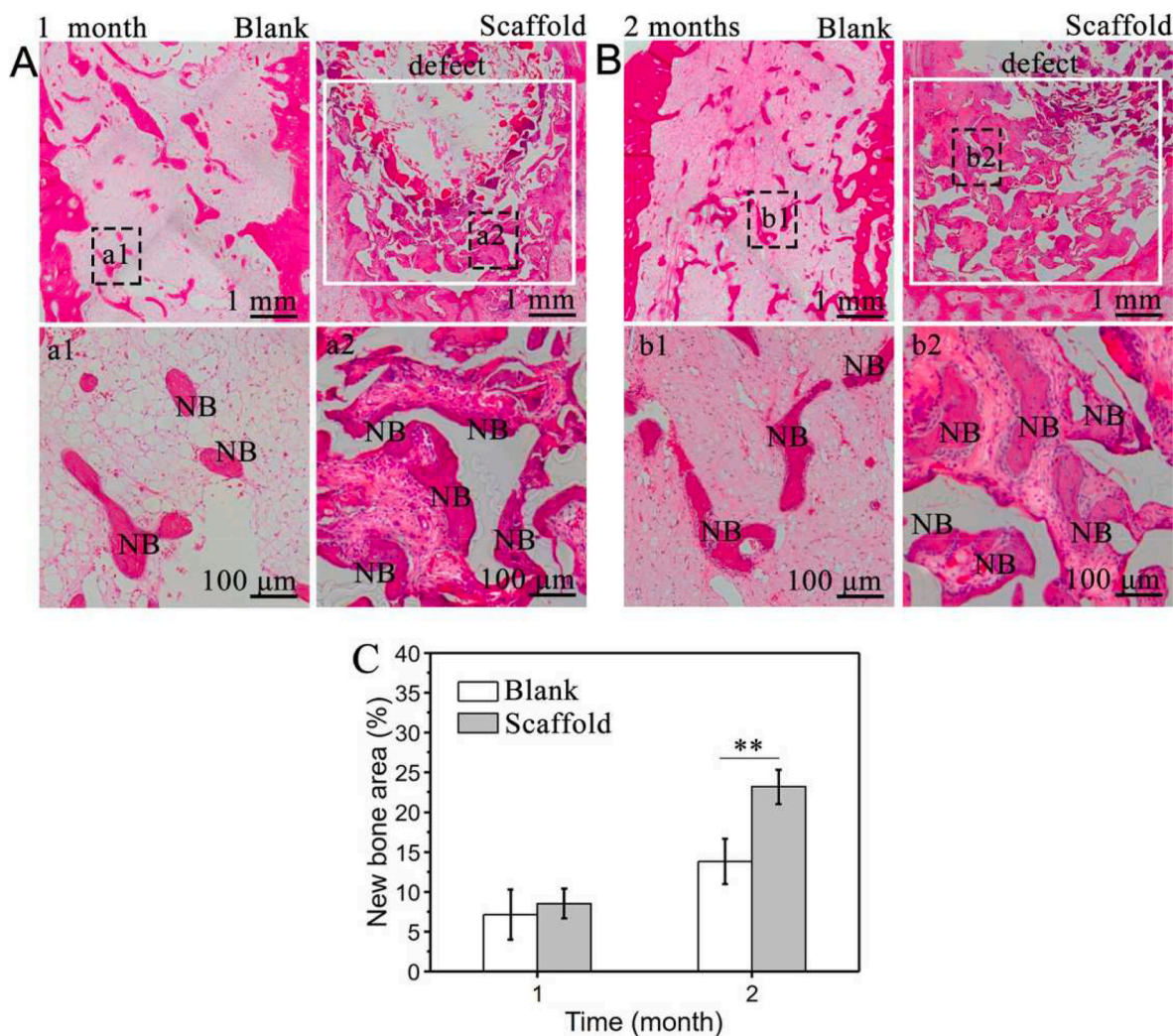
Fig. 10. Histological analysis of regenerated alveolar bone of (stiffened scaffold)/PDA/0.1Ag/HA (scaffold group) or left unfilled (blank group). H&E staining images after (A) 1 month and (B) 2 months. (a1), (a2) and (b1), (b2) are the magnification in (A) and (B), respectively. (C) New bone area percentage calculated by H&E staining. All statistical data are represented as mean ± SD (n = 3, **$P < 0.01$).

vivo degradation, anti-bacterial activity, cytotoxicity, stem cell proliferation and osteogenic differentiation revealed that this SM polymer possessed the optimal comprehensive performance as an implantable scaffold. Importantly, these scaffolds boosted efficient alveolar bone regeneration *in vivo*. The prepared scaffold with multi-functions was promising for alveolar bone regeneration.

4. Experimental section

4.1. Materials

PLGA ($M_n = 1.0 \times 10^5$ g mol^{-1}) was synthesized in our lab. Stannous octoate (Sn(Oct)$_2$), *N*-hydroxysuccinimide (NHS), 4-dimethylaminopyridine (DMAP), acryloyl chloride (AC), ε-caprolactone (ε-CL), ω-pentadecalactone (ω-PDL), 2,2-bimethoxy-2-phenylacetophenone (DMPA) were purchased from Aladdin Reagent Co., Ltd. Hydroxyethyl methacrylate (HEMA), 1,3-propanediol (PDO), triethylamine (TEA), dichloromethane (DCM), NaCl, dopamine hydrochloride, AgNO$_3$, sodium dihydrogen phosphate and calcium chloride were purchased from Sinopharm Chemical Reagent Co., Ltd.

4.2. Synthesis of polymers

PLGA-*g*-PCL: HEMA-PCL was grafted on PLGA through esterification reaction to obtain PLGA-*g*-PCL and synthesis was described as follows. HEMA-PCL was synthesized by ring opening polymerization of ε-CL initiated by HEMA and catalyzed by Sn(Oct)$_2$. The molar ratio of ε-CL to HEMA was set at 30:1. After reacted for 12 h at 120 °C in anhydrous toluene, HEMA-PCL was obtained by precipitation in cold ether and purification. Then, PLGA (0.02 g, 0.16 mmol), HEMA-PCL (0.35 g, 0.10 mmol) were dissolved in DMSO (20 mL) followed by addition of EDC·HCl (0.08 g, 0.4 mmol) and DMAP (0.03 g, 0.26 mmol). The grafting ratio was set was 60%. After reacted for 6 h at 50 °C, the mixture was dialyzed in distilled water for 2 days. Finally, the product was collected by lyophilization.

PPDLDA: PPDL was modified by AC to obtain PPDLDA and a typical synthetic process was given as follows. PDO (0.18 g, 2.4 mmol) was applied to initiate ring-opening polymerization of ω-PDL (5.6 g, 24 mmol) and the reaction was catalyzed by 2 M DPP in anhydrous toluene. After reacting for 96 h at 80 °C, PPDL was poured in cold ether, precipitated and purified. Then, PPDL (3.2 g, 1 mmol), AC (0.18 g, 2 mmol) and TEA (0.4 g, 4 mmol) were added to anhydrous toluene and the reaction was carried out for 3 h at 80 °C. The mixture was filtrated to remove the salt and precipitated in cold ether. PPDLDA was finally

obtained after purification.

4.3. Fabrication of (stiffened scaffold)/PDA/Ag/HA

The (stiffened scaffold)/PDA/Ag/HA was fabricated by UV cross-linking, SCPL and hybrid coating methods. The fabrication procedure was given as follows. First, NaCl particles of 450–600 μm in diameter were mixed with distilled water and dried in a tube to form a template [21]. PLGA-*g*-PCL and PPDLDA were dissolved in DCM with 1 wt% DMPA as a photoinitiator. Then, the solution was added to the tube and centrifuged (1000 rpm, 1 min) to thoroughly mixed with NaCl template. PLGA-*g*-PCL and PPDLDA were chemically cross-linked under UV irradiation (50 W, 5 min). The porous stiffened scaffold was obtained by dialysis in water/alcohol (1:1) mixture for 2 days to remove NaCl. PLGA-*g*-PCL and PPDLDA with a mass ratio of 1:9, 3:7, 5:5, 7:3 and 9:1 was fabricated to get the T_r close to 37 °C. After that, the hybrid coating of PDA/Ag/HA was gradually deposited on the scaffold surface according to the literature [15,16]. The scaffold was immersed in the dopamine/Tris-HCl (2 mg mL^{-1}, pH 8.5) for 12 h PDA deposition, in AgNO$_3$ solution (0.1, 1 and 10 mM) for 4 h Ag deposition and in 10 × SBF solution for 12 h HA biomineralization. The scaffold was washed 3 times after every deposition procedure and finally obtained by lyophilized.

4.4. Characterization of the scaffolds

The porous structure and surface morphology of the scaffolds was recorded by SEM (JXA-840, JEOL, Japan). The pore size was calculated with the Nano-measure software. The gel fraction test was applied to evaluate the cross-linking density of the scaffolds [22]. Scaffolds (5 × 5 × 5 mm) were weighed and marked as M_0. Then, the samples were immersed in dichloromethane at room temperature. Dichloromethane was changed every 6 h to remove unreacted polymers. After 24 h, the samples were dried under vacuum until the mass remained unchanged, weighed and marked as M_1. The gel fraction was calculated according to the formula M_1/M_0. DSC (Q800, TA, USA) was used to detect the thermal property of the scaffolds under a continuous nitrogen purge. The PDA/Ag/HA hybrid coating was analyzed by EDX (JXA-840, JEOL, Japan), XRD (D\max- 2550, Rigaku Industrial Corporation, Japan) and TGA (Q500, TA, USA) to detect its element content, crystal structure and weight percentage. The mechanical strength of the scaffolds (5 × 5 × 5 mm) was measured by DMA (Q800, TA, USA) and the compression rate was set as 50% min^{-1}.

4.5. Shape memory properties

Scaffolds (5 × 5 × 5 mm) (were applied to determined R_f and R_r by DMA. The scaffold was heated at 37 °C for 5 min, compressed (80%, ε_d) at a rate of 50% min^{-1}, kept at 0 °C for 1 min (ε_f) and then reheated to 37 °C for recovery (ε_r). The R_f and R_r were calculated by equations (1) and (2):

$$R_f = \frac{\varepsilon_f}{\varepsilon_d} \times 100\% \tag{1}$$

$$R_r = \frac{\varepsilon_f - \varepsilon_r}{\varepsilon_r} \times 100\% \tag{2}$$

4.6. In vivo degradation

The sterilized scaffolds (5 × 5 × 3 mm) were implanted in the back of mice. Three samples were implanted in each rat. After 1, 2 and 3 months, the mice were euthanized, the samples were collected and stored in 4% paraformaldehyde at 4 °C. Histological analysis was performed by H&E staining. The remaining weight of the scaffold was measured after removing the tissue around them by immersion in 5.25% NaClO [41].

4.7. Ag$^+$ release and cytotoxicity

(Stiffened scaffold)/PDA/Ag/HA (5 × 5 × 3 mm) was immersed in 3 mL phosphate-buffered saline (PBS) at 37 °C. The solution was harvested and the concentration of Ag$^+$ was detected by Inductively Coupled Plasma (ICP). BMSCs were seeded on (Stiffened scaffold)/PDA/Ag/HA (5 × 5 × 3 mm) and cultured for 1, 3 and 7 days. The cytotoxicity of Ag$^+$ was detected by the DNA contents through Hoechst 33258 as previously reported [19].

4.8. Anti-bacterial tests

(Stiffened scaffold)/PDA/Ag/HA (Φ6 × 3 mm) was put on the surface of the 10 mL nutrient agars with 1 mL of *S. aureus* suspension in 0.9% NaCl (10^4 CFU mL^{-1}) through pouring method. The inhibition zone after 24 h incubation at 37 °C was recorded to prove the antibacterial activity of the Ag-loaded scaffolds. The bacterial inhibition ratio was done as follows. Typically, scaffolds (5 × 5 × 3 mm) were immersed in 1 × 10^5 CFU mL^{-1} bacterial suspensions for 24 h. The bacterial solution without any treatment was set as negative control, respectively. the optical density was detected at 600 nm by using a microplate reader (SAF-6801, BAJIU Corporation, Shanghai, China). Bacterial inhibition rate (%) = (B$_{Control}$-B$_{scaffold}$)/B$_{Control}$ × 100%. The *S. aureus* attachment on scaffolds were observed by LCM and SEM. Scaffolds (5 × 5 × 3 mm) were cultured with 2 mL of bacterial suspension in centrifuge tubes at 37 °C for 24 h. For LCM observation, samples were washed 3 times gently, fixed with 4% paraformaldehyde for 10 min, washed 3 times again and finally stained with DAPI in the dark. For SEM observation, samples were dehydrated and evaporated under vacuum after being fixed with 4% paraformaldehyde at 4 °C overnight.

4.9. Cell proliferation and osteogenic differentiation

BMSCs were seeded on the scaffolds (5 × 5 × 3 mm) to characterize cell proliferation after 1, 7 and 14 days. Cells were labeled with fluorescent 3,3′-dioctadecyloxacarbocyanine perchlorate (DiO) dye (Molecular Probes, USA) and observed by LCM. In addition, cell morphology was recorded by SEM. Proliferation of cells was detected by DNA assay with Hoechst 33258 dye (Yeasen, China). The fluorescence intensity at 465 nm was read on a microplate reader.

BMSC/scaffold composites were cultured in osteoinductive medium for 7 and 14 days. After that, RT-PCR and ARS staining were carried out to evaluate the osteogenic differentiation and calcium nodules. RNA was extracted and ARS staining was carried out by instructions. The relative gene quantity at day 1 was set as 1. The primer sequences are listed in Table S5. After incubation for 10 min at room temperature, the excess of ARS staining was washed with distilled water. The samples were air-dried and images were acquired with a camera.

4.10. Live/dead staining of BMSCs after loading

Cell viability on the (stiffened scaffold)/PDA/Ag/HA and (unreinforced scaffold)/PDA/Ag/HA under 50 g loading were observed using a Calcein-AM/PI double staining Kit (DOJINDO, Kumamoto, Japan). In brief, scaffolds (5 × 5 × 3 mm) were placed in 6-well hanging cell culture polyethylene terephthalate inserts with pore size of 1.0 μm (Millicell, Burlington, MA) and seeded with BMSCs. After 1-day culture, 50 g metal weights were placed on the thin cover slip to apply compressive force to the BMSC/scaffold composites. After loading for 12 h, the scaffold was washed with PBS and incubated using Calcein-AM (2 μmol/L) and PI (4.5 μmol/L). Fifteen minutes later, LCM was used to record the cell viability. Three scaffolds in each group were tested and the cell viability were calculated by the ratio of fluorescence intensity of living cells and dead cells using Image J software.

4.11. In vivo evaluation of alveolar bone regeneration

All procedures involved in treating animals including surgery were carried out in accordance with protocols approved by the Shanghai Stomatological Hospital of Fudan University.

Rabbits were used as the animal model for the study. The surgery was performed in rabbits under general anesthesia using the nose cone method to deliver 2% isoflurane/100% O_2. Following the extraction of the first premolar of mandible on both sides, the socket was enlarged to a critical-sized defect of $5 \times 5 \times 6$ mm. The defect was filled with a deformed shape memory scaffold ($6 \times 6 \times 5$ mm) as the scaffold group or left unfilled as the blank group. Samples were collected after 1 and 2 months for micro-CT measurement and histological examination.

The harvested bone specimens were imaged with micro-CT (Scanco Medical, Bassersdorf, Switzerland) with 70 kV voltage tension, 114 mA tube current and 700 ms of integration time. BV/TV, BMD and Tb.N were calculated.

After micro-CT analysis, samples were used for histological examination. Samples were fixed in 4% paraformaldehyde at 4 °C overnight, decalcified, embedded in paraffin, sectioned and deparaffinized with xylene followed by hydration in ethanol solutions of decreasing concentrations (100%–70%) for H&E staining. The histological images were captured under a microscope and new bone area was calculated for quantification.

4.12. Statistical analysis

All the tests were based on three independent samples. Data are presented as mean ± standard deviation. Student's t-test assuming equal variance was performed with the SPSS 10.0 software. A p-value less than 0.05 was considered statistically significant.

Ethics approval and consent to participate

All procedures involved in treating animals including surgery were carried out in accordance with protocols approved by the Shanghai Stomatological Hospital of Fudan University.

CRediT authorship contribution statement

Weijun Zhang: Materials preparation, evaluation, Formal analysis, Software, Writing – original draft. **Meilin Yu:** Animal experiment, Formal analysis, Software. **Yongqiang Cao:** Assisted in evaluating of materials. **Zihan Zhuang:** Assisted in evaluating of materials. **Kunxi Zhang:** Supervision, Writing – review & editing. **Dong Chen:** Project administration, Funding acquisition. **Wenguang Liu:** Supervision, Writing – review & editing. **Jingbo Yin:** Supervision, Conceptualization, Project administration, Writing – review & editing, Funding acquisition.

Declaration of competing interest

The authors declare no conflict of interest.

Appendix A. Supplementary data

Supplementary data to this article can be found online at https://doi.org/10.1016/j.bioactmat.2022.08.030.

References

[1] J.S. Seibert, H. Salam, Alveolar ridge preservation and reconstruction, Periodontology 11 (1996) 69–84.

[2] F. Van der Weijden, F. Dell'Acqua, D.E. Slot, Alveolar bone dimensional changes of post-extraction sockets in humans: a systematic review, J. Clin. Periodontol. 36 (2009) 1048–1058.

[3] M.D. Hager, S. Bode, C. Weber, U.S. Schubert, Shape memory polymers: past, present and future developments, Prog. Polym. Sci. 49–50 (2015) 3–33.

[4] Q. Zhao, H.J. Qi, T. Xie, Recent progress in shape memory polymer: new behavior, enabling materials, and mechanistic understanding, Prog. Polym. Sci. 49–50 (2015) 79–120.

[5] S. Di, X. Liu, D. Liu, T. Gong, S. Lu, S. Zhou, A multifunctional porous scaffold with capacities of minimally invasive implantation, self-fitting and drug delivery, Mater. Today Chem. 1–2 (2016) 52–62.

[6] X. Liu, K. Zhao, T. Gong, J. Song, C. Bao, E. Luo, J. Weng, S. Zhou, Delivery of growth factors using a smart porous nanocomposite scaffold to repair a mandibular bone defect, Biomacromolecules 15 (2014) 1019–1030.

[7] L.N. Woodard, K.T. Kmetz, A.A. Roth, V.M. Page, M.A. Grunlan, Porous poly (epsilon-caprolactone)-poly(l-lactic acid) semi-interpenetrating networks as superior, defect-specific scaffolds with potential for cranial bone defect repair, Biomacromolecules 18 (2017) 4075–4083.

[8] D. Zhang, O.J. George, K.M. Petersen, A.C. Jimenez-Vergara, M.S. Hahn, M. A. Grunlan, A bioactive "self-fitting" shape memory polymer scaffold with potential to treat cranio-maxillo facial bone defects, Acta Biomater. 10 (2014) 4597–4605.

[9] B. Zhang, J.E. DeBartolo, J. Song, Shape recovery with concomitant mechanical strengthening of amphiphilic shape memory polymers in warm water, ACS Appl. Mater. Interfaces 9 (2017) 4450–4456.

[10] B. Zhang, J.D. Skelly, J.R. Maalouf, D.C. Ayers, J. Song, Multifunctional scaffolds for facile implantation, spontaneous fixation, and accelerated long bone regeneration in rodents, Sci. Transl. Med. 11 (2019) 7411.

[11] Z. Jiang, H. Azim, R.A. Gross, Lipase-catalyzed copolymerization of ω-pentadecalactone with p-dioxanone and characterization of copolymer thermal and crystalline properties, Biomacromolecules 8 (2007) 2262–2269.

[12] P. Chen, Z. Wu, A. Leung, X. Chen, E. Landao-Bassonga, J. Gao, L. Chen, M. Zheng, F. Yao, H. Yang, L. Lidgren, B. Allan, Y. Liu, T. Wang, M. Zheng, Fabrication of a silver nanoparticle-coated collagen membrane with anti-bacterial and anti-inflammatory activities for guided bone regeneration, Biomed. Mater. 13 (2018), 065014.

[13] R. Yee, C. Holmgren, J. Mulder, D. Lama, D. Walker, W. van Palenstein Helderman, Efficacy of silver diamine fluoride for arresting caries treatment, J. Dent. Res. 88 (2009) 644–647.

[14] L. Pauksch, S. Hartmann, M. Rohnke, G. Szalay, V. Alt, R. Schnettler, K.S. Lips, Biocompatibility of silver nanoparticles and silver ions in primary human mesenchymal stem cells and osteoblasts, Acta Biomater. 10 (2014) 439–449.

[15] M. Li, X. Liu, Z. Xu, K.W. Yeung, S. Wu, Dopamine modified organic-inorganic hybrid coating for antimicrobial and osteogenesis, ACS Appl. Mater. Interfaces 8 (2016) 33972–33981.

[16] K. Xie, Z. Zhou, Y. Guo, L. Wang, G. Li, S. Zhao, X. Liu, J. Li, W. Jiang, S. Wu, Y. Hao, Long-term prevention of bacterial infection and enhanced osteoinductivity of a hybrid coating with selective silver toxicity, Adv. Healthc Mater. 8 (2019), 1801465.

[17] Y. Yang, Y. Cheng, F. Deng, L. Shen, Z. Zhao, S. Peng, C. Shuai, A bifunctional bone scaffold combines osteogenesis and antibacterial activity via in situ grown hydroxyapatite and silver nanoparticles, Bio-Des. Manuf. 4 (2021) 452–468.

[18] K.X. Zhang, L. Song, J. Wang, S. Yan, G. Li, L. Cui, J. Yin, Strategy for constructing vascularized adipose units in poly(L-glutamic acid) hydrogel porous scaffold through inducing in-situ formation of ASCs spheroids, Acta Biomater. 51 (2017) 246–257.

[19] W. Zhang, K. Zhang, G. Li, S. Yan, L. Cui, J. Yin, Effects of large dimensional deformation of a porous structure on stem cell fate activated by poly(l-glutamic acid)-based shape memory scaffolds, Biomater. Sci. 6 (2018) 2738–2749.

[20] C. Tong, J.A.J. Wondergem, D. Heinrich, R.E. Kieltyka, Photopatternable, branched polymer hydrogels based on linear macromonomers for 3D cell culture applications, ACS Macro Lett. 9 (2020) 882–888.

[21] D. Zhang, W.L. Burkes, C.A. Schoener, M.A. Grunlan, Porous inorganic-organic shape memory polymers, Polymer 53 (2012) 2935–2941.

[22] Y. Liu, Y. Li, G. Yang, X. Zheng, S. Zhou, Multi-stimulus-responsive shape-memory polymer nanocomposite network cross-linked by cellulose nanocrystals, ACS Appl. Mater. Interfaces 7 (2015) 4118–4126.

[23] J. Zotzmann, M. Behl, Y. Feng, A. Lendlein, Copolymer networks based on poly (ω-pentadecalactone) and poly(ε-caprolactone) segments as a versatile triple-shape polymer system, Adv. Funct. Mater. 20 (2010) 3583–3594.

[24] Y. Zhang, J. Hu, X. Zhao, R. Xie, T. Qin, F. Ji, Mechanically robust shape memory polyurethane nanocomposites for minimally invasive bone repair, ACS Appl. Bio Mater. 2 (2019) 1056–1065.

[25] L. Chen, J.X. Wang, C.Y. Tang, D.Z. Chen, W.C. Law, Shape memory effect of thermal-responsive nano-hydroxyapatite reinforced poly-D-L-lactide composites with porous structure, Compos. B Eng. 107 (2016) 67–74.

[26] J. Zhou, H. Li, W. Liu, R. Dugnani, R. Tian, W. Xue, Y. Chen, Y. Guo, H. Duan, H. Liu, A facile method to fabricate polyurethane based graphene foams/epoxy/carbon nanotubes composite for electro-active shape memory application, Compos. Part A Appl. Sci. Manuf. 91 (2016) 292–300.

[27] J. Yu, H. Xia, A. Teramoto, Q.Q. Ni, The effect of hydroxyapatite nanoparticles on mechanical behavior and biological performance of porous shape memory polyurethane scaffolds, J. Biomed. Mater. Res. 106 (2018) 244–254.

[28] H.-M. Ye, S.-F. Yao, Supernucleating role of poly(ω-pentadecalactone) during the crystallization of poly(ε-caprolactone) composites, Ind. Eng. Chem. Res. 56 (2017) 13725–13733.

[29] H. Lee, S.M. Dellatore, W.M. Miller, P.B. Messersmith, Mussel-inspired surface chemistry for multifunctional coatings, Science 318 (2007) 426–430.

[30] C. Shuai, Y. Xu, P. Feng, G. Wang, S. Xiong, S. Peng, Antibacterial polymer scaffold based on mesoporous bioactive glass loaded with in situ grown silver, Chem. Eng. J. 374 (2019) 304–315.

[31] M. Li, Q. Liu, Z. Jia, X. Xu, Y. Shi, Y. Cheng, Y. Zheng, Polydopamine-induced nanocomposite Ag/CaP coatings on the surface of titania nanotubes for antibacterial and osteointegration functions, J. Mater. Chem. B 3 (2015) 8796–8805.

[32] A.C. Tas, S.B. Bhaduri, Rapid coating of Ti6Al4V at room temperature with a calcium phosphate solution similar to 10× simulated body fluid, J. Mater. Res. 19 (2011) 2742–2749.

[33] G. Iviglia, C. Cassinelli, E. Torre, F. Baino, M. Morra, C. Vitale-Brovarone, Novel bioceramic-reinforced hydrogel for alveolar bone regeneration, Acta Biomater. 44 (2016) 97–109.

[34] D.C. Stanton, J.C. Chou, L.R. Carrasco, Injectable calcium-phosphate bone cement (Norian) for reconstruction of a large mandibular defect: a case report, J. Oral Maxillofac. Surg. 62 (2004) 235–240.

[35] J. Fu, C. Wiraja, H.B. Muhammad, C. Xu, D.A. Wang, Improvement of endothelial progenitor outgrowth cell (EPOC)-mediated vascularization in gelatin-based hydrogels through pore size manipulation, Acta Biomater. 58 (2017) 225–237.

[36] F.J. O'Brien, Biomaterials & scaffolds for tissue engineering, Mater, Today Off. 14 (2011) 88–95.

[37] X.F. Zhang, Z.G. Liu, W. Shen, S. Gurunathan, Silver nanoparticles: synthesis, characterization, properties, applications, and therapeutic approaches, Int. J. Mol. Sci. 17 (2016) 1534.

[38] K. Chen, K. Xie, Q. Long, L. Deng, Z. Fu, H. Xiao, L. Xie, Fabrication of core–shell Ag@pDA@HAp nanoparticles with the ability for controlled release of Ag+ and superior hemocompatibility, RSC Adv. 7 (2017) 29368–29377.

[39] C. Ning, X. Wang, L. Li, Y. Zhu, M. Li, P. Yu, L. Zhou, Z. Zhou, J. Chen, G. Tan, Y. Zhang, Y. Wang, C. Mao, Concentration ranges of antibacterial cations for showing the highest antibacterial efficacy but the least cytotoxicity against mammalian cells: implications for a new antibacterial mechanism, Chem. Res. Toxicol. 28 (2015) 1815–1822.

[40] W. Liao, M. Okada, K. Inami, Y. Hashimoto, N. Matsumoto, Cell survival and gene expression under compressive stress in a three-dimensional in vitro human periodontal ligament-like tissue model, Cytotechnology 68 (2016) 249–260.

[41] C.X. Lam, D.W. Hutmacher, J.T. Schantz, M.A. Woodruff, S.H. Teoh, Evaluation of polycaprolactone scaffold degradation for 6 months in vitro and in vivo, J. Biomed. Mater. Res. 90 (2009) 906–919.